Modification of the electrochemical activity of $LiMn_{1.95}Si_{0.05}O_4$ spinel via addition of phases with different physico-chemical properties.

Amaia Iturrondobeitia,[a] Aintzane Goñi,[a] Luis Lezama,[a] Chunjoong Kim,[b,c] Marca Doeff,[c] Jordi Cabana[b,c] and Teófilo Rojo*[a,d]

Received (in XXX, XXX) Xth XXXXXXXXX 20XX, Accepted Xth XXXXXXXXX 20XX
DOI: 10.1039/b000000x

We report the synthesis of composites based on freeze-dried $LiMn_{1.95}Si_{0.05}O_4$ spinel. In order to improve the active material-electrolyte interface for better cyclability, three different additive materials were chosen: $LiMn_{1.9}Ga_{0.1}O_4$, Al_2O_3 and Li_3PO_4. A morphologic examination of the composites demonstrated a good connection of the homogeneous primary particles about 50 nm in diameter and the different additive materials, especially when adding $LiMn_{1.9}Ga_{0.1}O_4$ and Al_2O_3. The nature of the additives was confirmed by XPS and magnetic measurements. The electrochemical study revealed that $LiMn_{1.9}Ga_{0.1}O_4$ is a suitable complement to $LiMn_{1.95}Si_{0.05}O_4$. Due to the similar transport properties, the concurrence of both differently substituted spinels in the electrode material has a synergistic effect favoring the electrochemical response of the cathode composite.

Introduction

Lithium manganese oxide spinel is one of the preferred materials for application in the cathode in lithium ion batteries (LIBs). It exhibits rapid Li extraction/insertion processes near 4V (vs. Li/Li^+), and is especially interesting for use in hybrid electric vehicles (HEVs) and electric vehicles (EVs) due to its low cost, low toxicity, ease of preparation

and favorable safety characteristics . [1] However, as mature as its application may be today, some serious shortcomings remain to be solved, especially with regards to capacity decay, both for more widespread commercialization and to reduce the cost penalty imposed by the engineering fixes that it requires at the battery pack level [2].The capacity fading is mainly attributed to three aspects: 1) a cooperative Jahn-Teller distortion that causes the deleterious formation of a tetragonal phase upon inadvertent over-reduction past the point where half of the Mn is in the trivalent oxidation state, 2) the progressive dissolution of Mn (III) in the electrolyte and, 3) the decomposition of the organic solvents from the electrolyte at high potentials.

To address these problems, one solution is to substitute a small portion of the Mn ions with divalent or trivalent cations such as Mg^{+2}, Ga^{+3}, Al^{+3}, Cu^{+2} or Cr^{+3} [3-6]. This decreases the amount of Mn (III) in the structure, and lessens the probability of producing the Jahn-Teller distorted tetragonal phase at the end of discharge. Unfortunately, the decrease in the amount of the oxidizable species also leads to a reduction of the specific capacity delivered in the 3.5-4.2 V range. Another solution is to substitute a small amount of Mn (IV) by a tetravalent dopant, such as Si (IV), in order to stabilize the spinel framework without decreasing the amount of the electroactive Mn (III) cation. A previous study showed that the presence of 0.05 mol of Si (IV) in the structure of $LiMn_2O_4$ induces more expanded and regular MnO_6 octahedra that can more readily accommodate the Mn(III)–Mn(IV) change [7]. The insertion of more than 0.05 mol of the tetravalent substituent, however, caused deterioration of the electrochemical behaviour [8].

Although ion substitution can improve the stability of the bulk (barrier 1 above), it is also important to minimize the amount of the active material-electrolyte interface for better cyclability (barriers 2 and 3). Towards this end, a variety of surface coatings have been investigated, including oxides, metals [9], fluorides [10], phosphates [11], polymers [12], carbon [13] and electrode active materials [14]. In the case of nanostructured materials, the high surface area may adversely impact the cycling performance. For that reason, the use of a suitable additive material can improve the cyclability.

In this study, nanosized $LiMn_2O_4$ was successfully substituted with a small amount of Si(IV) in order to stabilize the spinel framework. For increased durability, three different materials were chosen to form composites. These materials have different properties, which could create insight into the rules of design that they should follow, but the synthesis procedure was designed so that they all reduce the contact between the electrolyte and Mn (III) ions at the surface of the spinel. The first secondary component was $LiMn_{1.9}Ga_{0.1}O_4$, a phase that also crystallizes in a spinel structure. Previous studies showed that the substitution of 5% Ga(III) for Mn(III) in the structure improves cycling properties [7]. Furthermore, this compound should conduct both ions and electrons, and the structural resemblance between spinels is an advantage in terms of composite cohesion. The second material that was chosen is Al_2O_3. It is both an ionic and electronic insulator. It is also thought to scavenge hydrogen fluoride (HF) formed from side reactions in lithium ion batteries, and thereby slow down dissolution of manganese ions and degradation of electrolytes at the cathode (barriers 2 and 3) [15]. The last additive material

was Li_3PO_4. While also separating the spinel surface from the electrolyte, unlike Al_2O_3, this phosphate is a solid lithium ion conductor [16]. Based on considerations of shape and size of the Si (IV) substituted spinel nanoparticles and taking into account the densities of the additive materials ($LiMn_{1.9}Ga_{0.1}O_4$, Al_2O_3 and Li_3PO_4), it was estimated that appropriate amounts for the secondary phases were 50 wt%, 10 wt% and 10 wt% for $LiMn_{1.9}Ga_{0.1}O_4$, Al_2O_3 and Li_3PO_4, respectively. In this article we report on the magnetic, spectroscopic and electrochemical properties of these composites.

Experimental

Materials and reagents

The following materials and reagents were used as purchased without further purification: citric acid monohydrate (99.5 %, Sigma-Aldrich), manganese (III) acetate dihydrate (97 %, Sigma-Aldrich), lithium hydroxide monohydrate (99 %, Fluka), silicon acetate (99 %, Alfa Aesar), gallium nitrate (99.99 %, Sigma-Aldrich), aluminium acetate basic (99.99 %, Sigma-Aldrich), ammonium dihydrogen phosphate (99.5 %, Fluka) and ammonium hydroxide solution (28-30 %, Sigma-Aldrich).

Sample Preparation

$LiMn_{1.95}Si_{0.05}O_4$ was synthesized by a freeze-drying method. First, $C_6H_8O_7 \cdot H_2O$, $Mn(C_2H_3O_2)_3 \cdot 2H_2O$, $Si(CH_3COO)_4$, and $LiOH \cdot H_2O$ in a molar ratio of 3:1.95:0.05:1were dissolved in 25 ml of water. The resulting solution was subsequently frozen in a round-bottom flask that contained liquid nitrogen. Afterwards, the round bottom flask was

connected to the freeze-dryer for 48 h at a pressure of $3 \cdot 10^{-1}$ mbar and a temperature of -80ºC to sublime the solvent. The as-obtained precursor was subjected to a single heat treatment at 700ºC for 4h. Subsequently, the product was ball-milled for 30 minutes. The obtained $LiMn_{1.95}Si_{0.05}O_4$ powders were used as baseline reagent for the different composites.

In order to prepare the 50 wt% $LiMn_{1.9}Ga_{0.1}O_4$ / 50 wt% $LiMn_{1.95}Si_{0.05}O_4$ (**$LiMn_{1.95}Si_{0.05}O_4$_ $LiMn_{1.9}Ga_{0.1}O_4$**) composite, the as synthesized $LiMn_{1.95}Si_{0.05}O_4$ powders were also added to a homogeneous solution of $C_6H_8O_7 \cdot H_2O$, $Mn(C_2H_3O_2)_3 \cdot 2H_2O$, $Ga(NO_3)_3$ and $LiOH \cdot H_2O$ with a molar ratio of 3:1.9:0.1:1. The dispersion was subsequently freeze-dried and treated following the same procedure that was used for pure $LiMn_{1.95}Si_{0.05}O_4$.

The 10 wt% Al_2O_3 / 90 wt% $LiMn_{1.95}Si_{0.05}O_4$ composite (**$LiMn_{1.95}Si_{0.05}O_4$_Al_2O_3**) was synthesized using the electrostatic attraction forces between the spinel and the alumina [17]. A solution was prepared by mixing the aluminum acetate basic powders in 30 ml of water. The pH was adjusted to 6.7, which is the midpoint between the point of zero charge of the spinel and alumina, by using NH_4OH (28-30%, Sigma-Aldrich). Then, $LiMn_{1.95}Si_{0.05}O_4$ was added into the pH-controlled solution and stirred at 100ºC until the water was almost evaporated. The suspension was annealed at 500ºC for 2h. For the 90 wt% $LiMn_{1.95}Si_{0.05}O_4$ / 10 wt% Li_3PO_4 composite (**$LiMn_{1.95}Si_{0.05}O_4$_Li_3PO_4**), a stoichiometric solution of lithium hydroxide and ammonium dihydrogen phosphate was prepared. Then, $LiMn_{1.95}Si_{0.05}O_4$ was added and stirred at 100ºC until the water was

almost evaporated. The suspension was annealed at 300ºC for 3h.

Characterization

Structural characterization of the samples was performed by X-ray powder diffraction with a Bruker D8 Advance Vario diffractometer using CuK_α radiation. The obtained diffractograms were profile-fitted using the FullProf program [18]. The morphologies of the materials were observed by Transmission Electron Microscopy (TEM) using a FEI TECNAI F30 and by a scanning electron microscope (JEOL JSM 7500F). X-ray photo electron spectra (XPS) were obtained on an SPECS system equipped with a Phoibos 150 1D-DLD analyzer and a monochromatic AlK_α (1486.6 eV) source. Magnetic susceptibility measurements (dc) were carried out between 5K and 300K with a Quantum Design SQUID magnetometer.

2032 coin cells were assembled to evaluate the electrochemical performances of the samples. To prepare the electrodes the active materials were mixed with conducting carbon black (Super P, Timcal) and polyvinylidene fluoride (PVDF) binder with the weight ratio of 80:10:10 and dispersed in N-methyl-2-pyrrolidone (NMP) to form a slurry. The slurry was then cast onto Al current collectors and dried at 120ºC in a vacum oven overnight. Electrochemical cells with metallic lithium foil as the counter electrode, Celgard 2400 polypropylene separators and 1 M $LiPF_6$ in 50%-50% ethyl carbonate (EC) and dimethyl carbonate (DMC) as the electrolyte solution, were assembled in an Ar-filled glove box. All the electrochemical measurements were carried out on a Bio-Logic VMP3 potentiostat battery tester at room temperature. Typical electrode loadings were 1.3

mg/cm^2.

The galvanostatic charge/discharge experiments were performed between 3.5 and 4.3V at 0.1C and 1C current rates. 1C was based on full delithiation of samples, $LiMn_{1.95}Si_{0.05}O_4$ $\leftrightarrow$ $Li + Mn_{1.95}Si_{0.05}O_4$. To calculate the capacity values, only $LiMn_{1.95}Si_{0.05}O_4$ was considered as an active material in the composites with Al_2O_3 and Li_3PO_4. In addition, the rate capability of the materials was characterized through the acquisition of a "signature curve" (SC) [19], obtained by a protocol that consists of an initial charge performed at 0.1C followed by a series of successive discharges at different rates, from highest (10C) to lowest (0.1C), with relaxation periods of 5 min and no charging step in between.

Results and discussion

Figure 1 shows the XRD patterns of pure $LiMn_{1.95}Si_{0.05}O_4$ and composite samples. All of the major diffraction peaks could be indexed to the cubic spinel *Fd-3m* space group. Some weak reflections corresponding to Li_3PO_4 (Powder Diffraction File 84-0046 PDF card) were detected in the $LiMn_{1.95}Si_{0.05}O_4$_Li_3PO_4 composite and are marked with asterisks in the figure, but no additional reflections were detected for the rest of the samples. This fact implies that the Al_2O_3 must be in amorphous form. In the case of $LiMn_{1.95}Si_{0.05}O_4$_$LiMn_{1.9}Ga_{0.1}O_4$ sample, both materials exhibit very similar overlapped XRD patterns. The values obtained for cell parameters and volumes from profile-fittings are shown in Table 1. The value of the cell parameter exhibited very little variation between the pure $LiMn_{1.95}Si_{0.05}O_4$ and composite samples. However, it is not unreasonable to suspect that at the interface between the spinel and the additive phases

some ionic-mixing and disorder occurs.

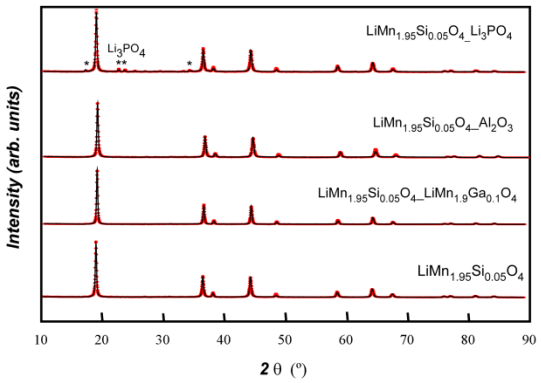

Figure.1 X-ray patterns of $LiMn_{1.95}Si_{0.05}O_4$ and composite samples.

Table 1 Cell parameters and volumes for $LiMn_{1.95}Si_{0.05}O_4$ and composite samples.

Sample	Cell parameter (Å)	Cell volume (Å^3)
$LiMn_{1.95}Si_{0.05}O_4$	8.2363(3)	558.72(1)
$LiMn_{1.95}Si_{0.05}O_4$_$LiMn_{1.9}Ga_{0.1}O_4$	8.2345(3)	558.36(1)
$LiMn_{1.95}Si_{0.05}O_4$_ Al_2O_3	8.2332(3)	558.09(1)
$LiMn_{1.95}Si_{0.05}O_4$_ Li_3PO_4	8.2330(3)	558.05(1)
$LiMn_{1.9}Ga_{0.1}O_4$*	8.2165(7)	554.71(1)

Values got from ref. 7

Figure 2a shows a transmission electron micrograph of $LiMn_{1.95}Si_{0.05}O_4$. The synthesis procedure and moderate annealing temperature resulted in homogeneous, primary particles about 50 nm in diameter. **Figures 2b, 2c and 2d** show the micrographs of the composite materials. In **Figure 2b,** the presence of segregated $LiMn_{1.9}Ga_{0.1}O_4$ particles

grown on the surface of crystalline $LiMn_{1.95}Si_{0.05}O_4$ show that there is good cohesion between the spinel phases. It is important to note that the particle size for $LiMn_{1.9}Ga_{0.1}O_4$ was smaller than that for $LiMn_{1.95}Si_{0.05}O_4$, as could be expected from the shorter annealing time at 700ºC for the former compared to the latter. The $LiMn_{1.95}Si_{0.05}O_4$_ Al_2O_3 micrograph, **Figure 2c**, shows the existence of a layer of Al_2O_3 on the spinel particle surfaces. The $LiMn_{1.95}Si_{0.05}O_4$_ Li_3PO_4 composite appeared to be more heterogeneous than the other two materials. In some areas pure $LiMn_{1.95}Si_{0.05}O_4$ was detected but in others, well crystallized Li_3PO_4 particles mixed with $LiMn_{1.95}Si_{0.05}O_4$ nanoparticles were found (**Figure 2d**).

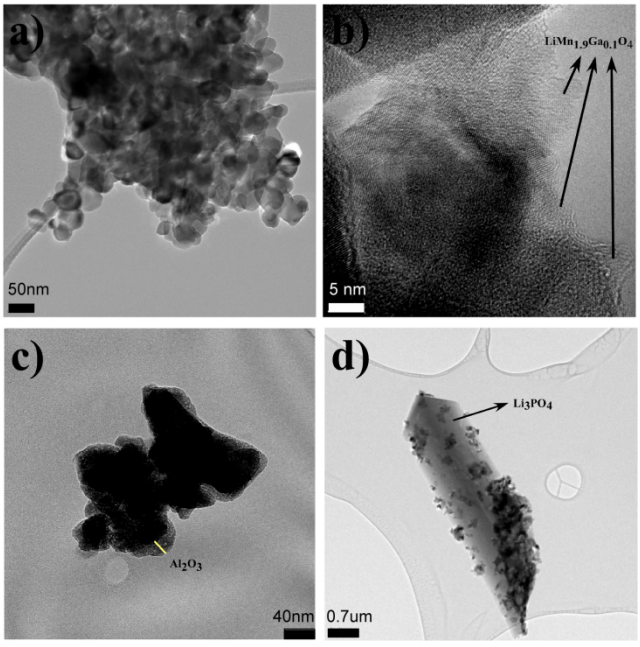

Figure2. TEM micrographs of a) $LiMn_{1.95}Si_{0.05}O_4$, b) $LiMn_{1.95}Si_{0.05}O_4$_$LiMn_{1.9}Ga_{0.1}O_4$, c) $LiMn_{1.95}Si_{0.05}O_4$_Al_2O_3 and d) $LiMn_{1.95}Si_{0.05}O_4$_ Li_3PO_4 samples.

Figures 3 a, b, c and d show the SEM images of $LiMn_{1.95}Si_{0.05}O_4$,

$LiMn_{1.95}Si_{0.05}O_4$_$LiMn_{1.9}Ga_{0.1}O_4$, $LiMn_{1.95}Si_{0.05}O_4$_ Al_2O_3 and $LiMn_{1.95}Si_{0.05}O_4$_ Li_3PO_4 powders. The overall morphologies of $LiMn_{1.95}Si_{0.05}O_4$_ $LiMn_{1.9}Ga_{0.1}O_4$ and $LiMn_{1.95}Si_{0.05}O_4$_ Al_2O_3 samples were similar to that of the pure $LiMn_{1.95}Si_{0.05}O_4$. On the other hand, **figure 3d** shows the presence of large crystals, probably Li_3PO_4, mixed with some $LiMn_{1.95}Si_{0.05}O_4$ particles.

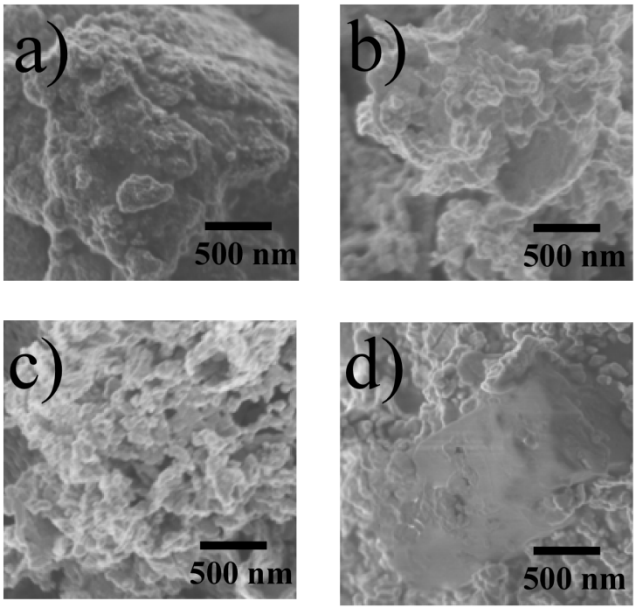

Figure 3. SEM images of a) $LiMn_{1.95}Si_{0.05}O_4$, b) $LiMn_{1.95}Si_{0.05}O_4$_$LiMn_{1.9}Ga_{0.1}O_4$, c) $LiMn_{1.95}Si_{0.05}O_4$_Al_2O_3 and d) $LiMn_{1.95}Si_{0.05}O_4$_ Li_3PO_4 samples.

XPS was used to study the surface composition of the composite samples. High resolution Ga $2p_{3/2}$ spectra for $LiMn_{1.95}Si_{0.05}O_4$ and $LiMn_{1.95}Si_{0.05}O_4$_$LiMn_{1.9}Ga_{0.1}O_4$

samples are shown in **figure 4**. In contrast to $LiMn_{1.95}Si_{0.05}O_4$, $LiMn_{1.95}Si_{0.05}O_4$_$LiMn_{1.9}Ga_{0.1}O_4$ spectra showed the presence of the Ga $2p_{3/2}$ signal due to the addition of $LiMn_{1.9}Ga_{0.1}O_4$. **Figures 5a and 5b** depict high resolution Al 2p and Mn 2p spectra for $LiMn_{1.95}Si_{0.05}O_4$ and $LiMn_{1.95}Si_{0.05}O_4$_Al_2O_3 samples. As a consequence of the Al_2O_3 layer, both a decrease in the Mn 2p band area and the emergence of an Al 2p signal were observed. High resolution P 2p and Mn 2p spectra are shown in **figures 6a and 6b** for $LiMn_{1.95}Si_{0.05}O_4$ and $LiMn_{1.95}Si_{0.05}O_4$_Li_3PO_4. Although the P 2p signal was detected for $LiMn_{1.95}Si_{0.05}O_4$_Li_3PO_4, the Mn 2p band remained as intense as in pure $LiMn_{1.95}Si_{0.05}O_4$ due to the existence of the areas that contain crystallized Li_3PO_4 particles mixed with $LiMn_{1.95}Si_{0.05}O_4$ nanoparticles.

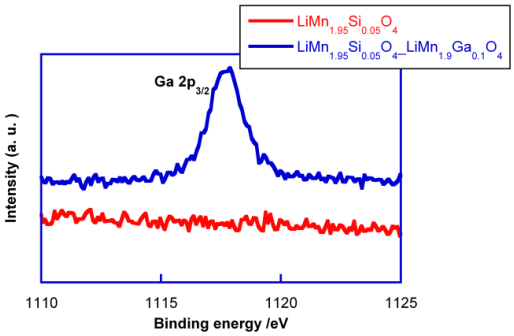

Figure 4. High resolution Ga $2p_{3/2}$ spectra for $LiMn_{1.95}Si_{0.05}O_4$ and $LiMn_{1.95}Si_{0.05}O_4$_$LiMn_{1.9}Ga_{0.1}O_4$ samples.

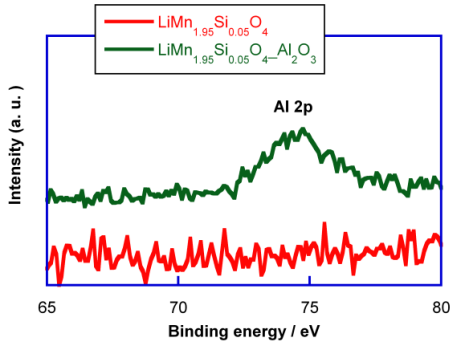

a)

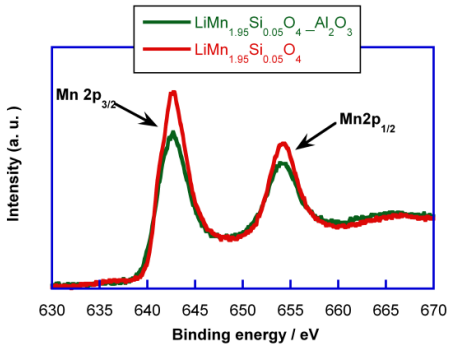

b)

Figure 5. High resolution Al 2p (a) and Mn 2p (b) spectra for $LiMn_{1.95}Si_{0.05}O_4$ and $LiMn_{1.95}Si_{0.05}O_4$_Al_2O_3 samples.

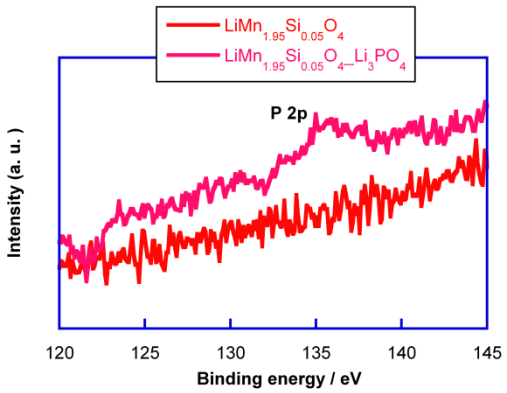

a)

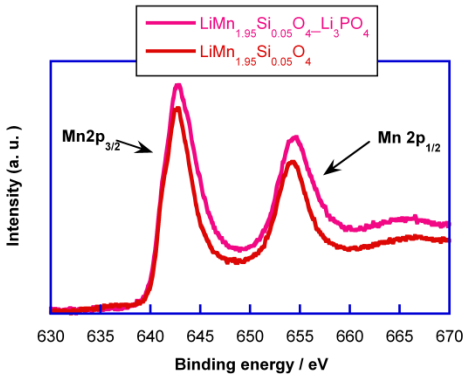

b)

Figure 6. High resolution P 2p (a) and Mn 2p (b) spectra for $LiMn_{1.95}Si_{0.05}O_4$ and $LiMn_{1.95}Si_{0.05}O_4$_Li_3PO_4 samples.

Magnetic susceptibility measurements on the $LiMn_{1.95}Si_{0.05}O_4$_$LiMn_{1.9}Ga_{0.1}O_4$ sample were carried out in the 5-300K temperature range at 100 Oe and 1 KOe. These measurements were not carried out for the rest of the samples as Al_2O_3 and Li_3PO_4 do not have any magnetic ions. The magnetic measurements of pure $LiMn_{1.95}Si_{0.05}O_4$ and $LiMn_{1.9}Ga_{0.1}O_4$ spinels were carried out in previous studies [7]. **Figure 7** shows the thermal evolution of χ_m for $LiMn_{1.95}Si_{0.05}O_4$_$LiMn_{1.9}Ga_{0.1}O_4$. The ZFC was indicative of predominantly antiferromagnetic interactions, but the FC curve diverges from 50 K showing the appearance of weak ferromagnetism below that temperature. As the inset of **figure 7** shows, the magnitude of the divergence was dependent on the applied field, becoming more pronounced at weaker magnetic fields. In addition, the use of a weaker

magnetic field allowed detailed observation of the maximum in χ_m. From here, the existence of two peaks that appear at 23 and 16 K could be deduced. As has been reported in previous studies by our group, the maximum at 23 K belongs to $LiMn_{1.95}Si_{0.05}O_4$ and the maximum at 16 K corresponds to $LiMn_{1.9}Ga_{0.1}O_4$ [7]. This result confirms the coexistence of both spinel phases in the composite material.

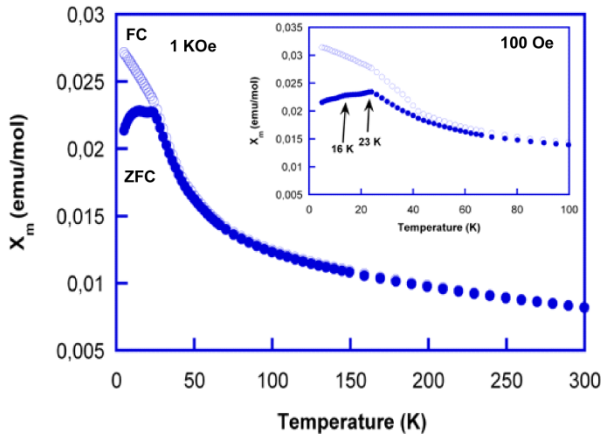

Figure 7. Thermal evolution of χ_m for $LiMn_{1.95}Si_{0.05}O_4$_$LiMn_{1.9}Ga_{0.1}O_4$

The magnetic sublattice in the spinel structure satisfies the condition of a magnetically frustrated system[20]. $LiMn_{1.95}Si_{0.05}O_4$_$LiMn_{1.9}Ga_{0.1}O_4$, showed a typical magnetic behavior of spinels with the presence of partially ordered magnetic clusters of different sizes [7,8]. The nature of the weak ferromagnetic component at low temperature, is a result of the disorder and the different short-range competing magnetic interactions in the composite.

To evaluate the electrochemical performance, lithium half-cells containing the pure

$LiMn_{1.95}Si_{0.05}O_4$ and composite materials were discharged at a current rate corresponding to C/10 and 1C. **Figure 8** shows the first discharge profiles of the samples at C/10 and 1C at room temperature. All discharge curves have two plateaus around 4.0 and 4.1 V, which indicate that the extraction and reinsertion of lithium ions from tetrahedral sites occurs in two steps. This behaviour is typical of $LiMn_2O_4$ and its variants [7,8]. The initial discharge capacity of $LiMn_{1.95}Si_{0.05}O_4$ sample was 122 mAh/g at C/10 and 104 mAh/g at 1C. As previously reported [7], the specific capacity delivered by $LiMn_{1.9}Ga_{0.1}O_4$ is only about 75% of that delivered by $LiMn_{1.95}Si_{0.05}O_4$. However the addition of $LiMn_{1.9}Ga_{0.1}O_4$ in a composite with $LiMn_{1.95}Si_{0.05}O_4$ did not result in the expected dropin capacity with respect to the pure sample, pointing at the existence of a synergistic effect between the two spinel phases.

However, when inactive Al_2O_3 or Li_3PO_4 were added, the capacity values decreased (see Table 2). Thus it could be said that the inclusion of redox inactive additive materials in the cathodic composite worked against that electrochemical parameter.

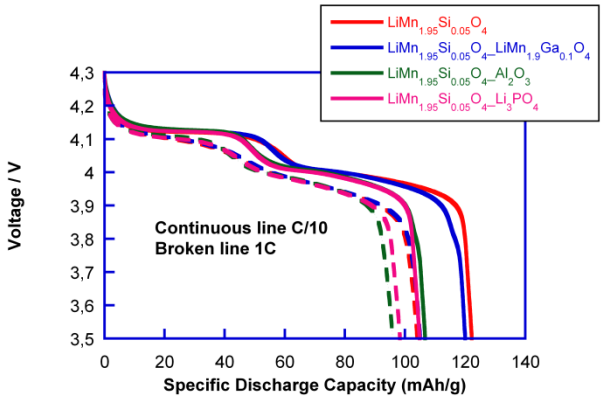

Figure 8. First discharge profiles of $LiMn_{1.95}Si_{0.05}O_4$ and composite samples at C/10 and 1C at room temperature.

Table 2 Specific discharge capacity values at C/10 and 1C for $LiMn_{1.95}Si_{0.05}O_4$ and composite samples

Sample	Specific Discharge Capacity C/10 (mAh/g)	Specific Discharge Capacity 1C (mAh/g)
$LiMn_{1.95}Si_{0.05}O_4$	122	104
$LiMn_{1.95}Si_{0.05}O_4$_Li $Mn_{1.9}Ga_{0.1}O_4$	120	105
$LiMn_{1.95}Si_{0.05}O_4$_ Al_2O_3	96	86
$LiMn_{1.95}Si_{0.05}O_4$_ Li_3PO_4	94	88

The rate capabilities of the samples were evaluated using signature curves [15]. The cumulative charge passed at each rate was taken as the capacity values for the given rate.

Figure 9 shows the modified Peukert plot of all the samples. Nanosized $LiMn_{1.95}Si_{0.05}O_4$ and $LiMn_{1.95}Si_{0.05}O_4$_$LiMn_{1.9}Ga_{0.1}O_4$ samples had the best rate performances, maintaining almost 90% of the initial capacity values at 10C. The rate capability of the $LiMn_{1.95}Si_{0.05}O_4$_Al_2O_3 composite, was inferior, most likely due to the fact that Al_2O_3 is a pure insulator for both electrons and lithium ions. The performance of the $LiMn_{1.95}Si_{0.05}O_4$_Li_3PO_4 sample was also poorer than that of the pure spinel or the spinel-spinel composite. Although Li_3PO_4 is a solid lithium conductor, the presence of large crystals of Li_3PO_4 in the $LiMn_{1.95}Si_{0.05}O_4$_Li_3PO_4 composite also proved disadvantageous.

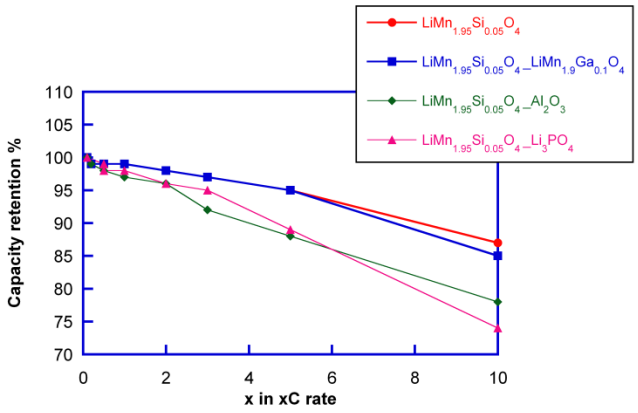

Figure 9. The modified Peukert plot of $LiMn_{1.95}Si_{0.05}O_4$, $LiMn_{1.95}Si_{0.05}O_4$_$LiMn_{1.9}Ga_{0.1}O_4$, $LiMn_{1.95}Si_{0.05}O_4$_Al_2O_3 and $LiMn_{1.95}Si_{0.05}O_4$_ Li_3PO_4 samples.

Figure 10 depicts the cycling performance of the samples. After 100 cycles at 1C, the

capacity retention of all materials was near 100%. However, after 300 cycles a slightly better capacity retention was observed for $LiMn_{1.95}Si_{0.05}O_4$_$LiMn_{1.9}Ga_{0.1}O_4$ (inset of figure 10) in comparison to the other materials. It could be said that since the Ga substituted spinel has less Mn (III), it provides some profit for pure $LiMn_{1.95}Si_{0.05}O_4$ spinel and enhances the cycling performance of the cathodic composite.

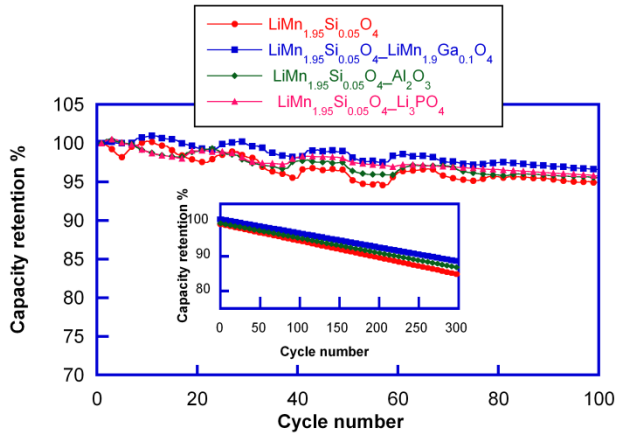

Figure 10. Cycling performance of $LiMn_{1.95}Si_{0.05}O_4$ and composite samples.

Figure 11 shows the coulombic efficiencies (defined as the ratio between discharge and charge capacity) of all the samples. The $LiMn_{1.95}Si_{0.05}O_4$_Al_2O_3 composite had the highest coulombic efficiency, with a value close to 100%. This could be ascribed to the presence of Al_2O_3, that as well as being both an ionic and electronic insulator, it scavenges the hydrogen fluoride [11] that has been formed from side reactions involving the electrolytic solution during charge and discharge processes. It is also possible that the apparently more conformal coating when using the oxide compared to Li_3PO_4 forms a better physical barrier to contact with acidic impurities. This way, the dissolution of the

manganese ions and the degradation of the electrolyte at the cathode are slowed down, improving the coulombic efficiency.

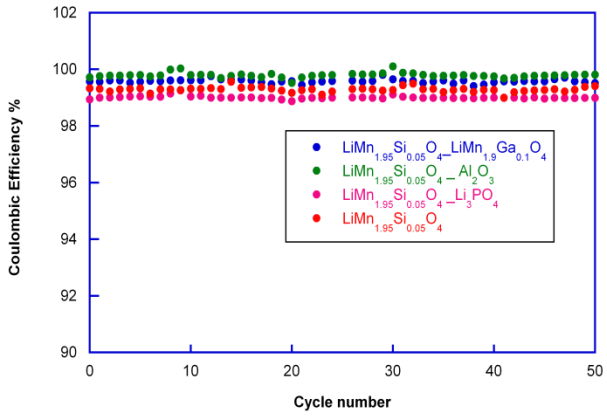

Figure 11. C oulombic efficiencies of $LiMn_{1.95}Si_{0.05}O_4$ and composite samples.

Conclusions

$LiMn_{1.95}Si_{0.05}O_4$_ $LiMn_{1.9}Ga_{0.1}O_4$, $LiMn_{1.95}Si_{0.05}O_4$_Al_2O_3 and $LiMn_{1.95}Si_{0.05}O_4$_ Li_3PO_4 composites based on freeze-dried $LiMn_{1.95}Si_{0.05}O_4$ spinel were successfully prepared. Despite some weak reflections corresponding to Li_3PO_4 were detected for $LiMn_{1.95}Si_{0.05}O_4$_ Li_3PO_4, for the rest of the samples all of the diffraction peaks could be indexed to the cubic spinel *Fd-3m* space group. Due to the synthesis procedure and moderate annealing temperature, 50 nm primary particles were obtained. The morphologic study demonstrated the presence of the secondary components ($LiMn_{1.9}Ga_{0.1}O_4$, Al_2O_3 and Li_3PO_4) in the composite materials. XPS and magnetic

measurements also proved the presence of the additive materials in the composites. The electrochemical study revealed that the addition of non electronically conductive phases caused a deterioration in the rate capability and cycling performance of pure $LiMn_{1.95}Si_{0.05}O_4$ although they improved the coulombic efficiencies. The addition of $LiMn_{1.9}Ga_{0.1}O_4$, in contrast, enhanced the capacity retention of the pure silicon substituted spinel without adversely affecting the rate capability or the discharge capacity. The similarities in structure between the two spinel phases, is advantageous in terms of composite cohesion, and the conductive behavior of $LiMn_{1.9}Ga_{0.1}O_4$ have a synergistic effect favoring the electrochemical performance of the cathode material.

Acknowledgments

This work was financially supported by the Ministerio de Ciencia e Innovación (MAT2010-19442) and the Gobierno Vasco/Eusko Jaurlaritza (IT570-13, ETORTEK CICENERGIGUNE10, SAIOTEK S-PE12UN140). A.I. thanks the Gobierno Vasco/Eusko Jaurlaritza for a fellowship. CK, MMD and JC were supported by the Assistant Secretary for Energy Efficiency and Renewable Energy, Office of Vehicle Technologies of the U.S. Department of Energy under Contract No. DE-AC02-05CH11231.

Notes and references

[a] *Departamento de Química Inorgánica, Universidad del País Vasco UPV/EHU, P.O. Box 644, 48080, Bilbao, Spain.*

[b] *Department of Chemistry, University of Illinois at Chicago, Chicago, IL 60607, USA.*

[c] *Environmental Energy Technologies Division, Lawrence Berkeley National Laboratory, 1 Cyclotron Rd. MS62R0203, Berkeley, CA 94720-8168, USA*

[d]*CIC energiGUNE, Parque Tecnolóogico de Álava. Albert Einstein 48, 01510 Miñano, Álava, Spain. Tel: +34945 297 108; E-mail: trojo@cicenergigune.com*

[1] L. Xiong, Y. Xu, T. Tao, J. Song, J. B. Goodenough, J. Mater. Chem. 22 (2012) 24563.

[2]Scrosati B, Garche J (2010) J Power Sources 195: 2419

[3]M. Prabu, M. V. Raddy, S. Selvasekarapandian, G. V. Subba Rao, B. V.R. Chowdary, Electrochimica Acta 88 (2013) 745-755.

[4]D. Q. Liu, Z. Z. He, X. Q. Liu, Journal of Alloys and Compounds 440 (2007) 69-73.

[5]M. Javed Iqbal, S. Zahor, Journal of Power Sources 165 (2007) 393-397.

[6]J. L. Wang, Z. H. Li, J. Yang, J. J. Tang, J. J. Yu, W. B. Nie, G. T. Lei, Q. Z. Xiao, Elctrochimica Acta 75 (2012) 115-122.

[7] A. Iturrondobeitia, A. Goñi, V. Palomares, I. Gil de Muro, L. Lezama, T. Rojo, J. Power Sources 216 (2012) 482-488

[8]A. Iturrondobeitia, A. Goñi, L. Lezama, C. Kim, M. Doeff, J. Cabana, T. Rojo, J. of Materials Chemistry 1 (2013) 10857-10862.

[9] J. Tu, X. B. Zhao, G. S. Cao, J. P. Tu. T. J. Zhu, Mater Lett. 60 (2006) 3251.

[10] J. G. Li, X. M. He, R. S. Zhao, Trans. Nonferrous Met. Soc. China 17 (2007) 1324.

[11] D. Q. Liu, Z. Z. He, X. Q. Liu, Mater. Lett. 61 (2007) 4703.

[12]R. Vidu, P Stroeve, Ind. Eng. Chem. Res. 43 (2004) 3314.

[13] H. S. Moon, S. W. Lee, Y. K. Lee, J. W. Park, J. Power Sources 713 (2003) 119-121.

[14]S. C. Park, Y. M. Kim, S. C. Han, S. Ahn, C. H. Ku, J. Y. Lee, J. Power Sources 107 (2002) 42.

[15]D. Guan, J. A. Jeevarajan, Y. Wang, Nanoscale 3 (2011) 1465.

[16]X. Li, R. Yang, B. Cheng, Q. Hao, H. Xu, J. Yang, Y. Qian, Materials Letters 66 (2012) 168-171.

[17]W. K. Kim, D. W. Han, W. H. Ryu, S. J. Lim, H. S. Kwon, Electrochim. Acta 71 (2012) 17-21.

[18]J. Rodríguez-Carvajal, http://valmap.dfis.ull.es/fullprof/

index.php.

[19]M. Doyle, J. Newman, J. Reimers, J. Power Sources 52 (1994) 211.

[20]J.E.Greendan, N.P. Raju, A.S. Wills, C. Morin, S.M. Shaw, Chem. Mater. 10 (1998) 3058.